Optics and Lasers in Engineering 154 (2022) 107022

Contents lists available at ScienceDirect

Optics and Lasers in Engineering

journal homepage: www.elsevier.com/locate/optlaseng

High speed fringe projection for dynamic shape measurement using binary phase mask. Part 2: manufacture and test

Wen Guo, C.R. Coggrave, J.M. Huntley*, P.D. Ruiz

Loughborough University, Wolfson School of Mechanical, Electrical and Manufacturing Engineering, Loughborough LE11 3TU, United Kingdom

ARTICLE INFO

Keywords:
Fringe projection
scatter plate
phase mask
high speed
binary projection
real time

ABSTRACT

Dynamic measurement of object shape is now achievable at projection rates of up to 30,000 binary fringe patterns per second from a digital micromirror device (DMD) based projector. This two-part paper describes the design, manufacture and test of a binary phase mask in the projection system that produces high-quality greyscale fringes from the binary patterns, with much reduced phase noise compared to the projector defocus approach that has been used until now. Part 2 describes the experimental verification and characterization of the phase masks, manufactured using photolithography and dry etching from the design methods described in Part 1. The height distribution of two masks with point spread function (PSF) dimensions of 1×256 and 4×64 pixels were assessed using coherence scanning interferometry and contact surface profilometry. Phase noise was determined using standard temporal unwrapping fringe sequences and found to be 20–50% higher than a traditional 8-bit greyscale approach. The projector lens distortion has been observed, and the corresponding compensation method shown to significantly improve the quality of the projected fringes. Increasing the number of projector frames per camera frame reduced phase noise, to less than one-half the 8-bit values for a 10-slice sequence. Fringe image acquisition rates for the 1-slice and 10-slice sequences are up to 255 × and 25 × faster than for the 8-bit greyscale sequence, respectively. Finally, examples are presented of fringe patterns and wrapped phase maps from a high-speed system used to measure moving objects, with projection and acquisition rates of up to 9515 frames s^{-1}.

1. Introduction

Fringe projection has become one of the most popular techniques in 3D shape measurement due to its advantages of non-contact, high-precision, and full-field measurement. Phase-shifting and temporal phase unwrapping algorithms are typically used to provide independent co-ordinate data at each camera pixel, with high signal-to-noise ratio, but require a few tens of fringe patterns per measured 3D point cloud. Therefore, significant effort is currently being devoted to increasing the projection speed to allow high system throughput for applications such as dimensional quality control and metrology-assisted assembly.

Part 2 of this two-part paper describes the manufacture and test of a pair of phase masks that were designed according to the numerical procedures outlined in Part 1 [1]. The fabricated mask is positioned in front of the projector lens to produce an anisotropic image blur, allowing pseudo-sine-wave fringe patterns to be projected at frame rates over two orders of magnitude faster than obtained using conventional greyscale fringe patterns.

Section 2 of the paper describes the method of phase mask fabrication, and the results of the inspection of the masks by using both contact and non-contact measuring instruments. In Section 3, the results of projection experiments are introduced. Firstly, the size of the point spread function (PSF) and the strength of the DC peak (i.e., the un-diffracted component of the wavefront) formed by using the masks are observed. Secondly, projection of binary fringe sequences under different conditions is performed with different masks. This part aims to analyse the performance and quality of the masks by comparing the unwrapped phase errors over a range of projection distances, fringe densities, and fringe design methods. In addition, the influence of lens distortion is discussed, and a corresponding compensation approach is proposed and verified. Section 4 of this paper introduces results from a high-speed fringe projection system. The synchronised high-speed projector and camera devices are used to acquire images of patterns projected onto a moving object. The resulting wrapped phase maps from different projected image sequences demonstrate the improvement in the data quality obtained from moving targets using the phase masks with binary patterns. Finally, the conclusions and summary of the paper are given in the last section.

2. Manufacture and inspection of the phase mask

The binary phase mask patterns, designed by the methods described in [1], were applied to $50 \times 50 \times 3$ mm^3 fused silica substrates by pho-

* Corresponding author.
E-mail address: J.M.Huntley@lboro.ac.uk (J.M. Huntley).

https://doi.org/10.1016/j.optlaseng.2022.107022
Received 14 September 2021; Received in revised form 1 February 2022; Accepted 1 March 2022
Available online 2 April 2022

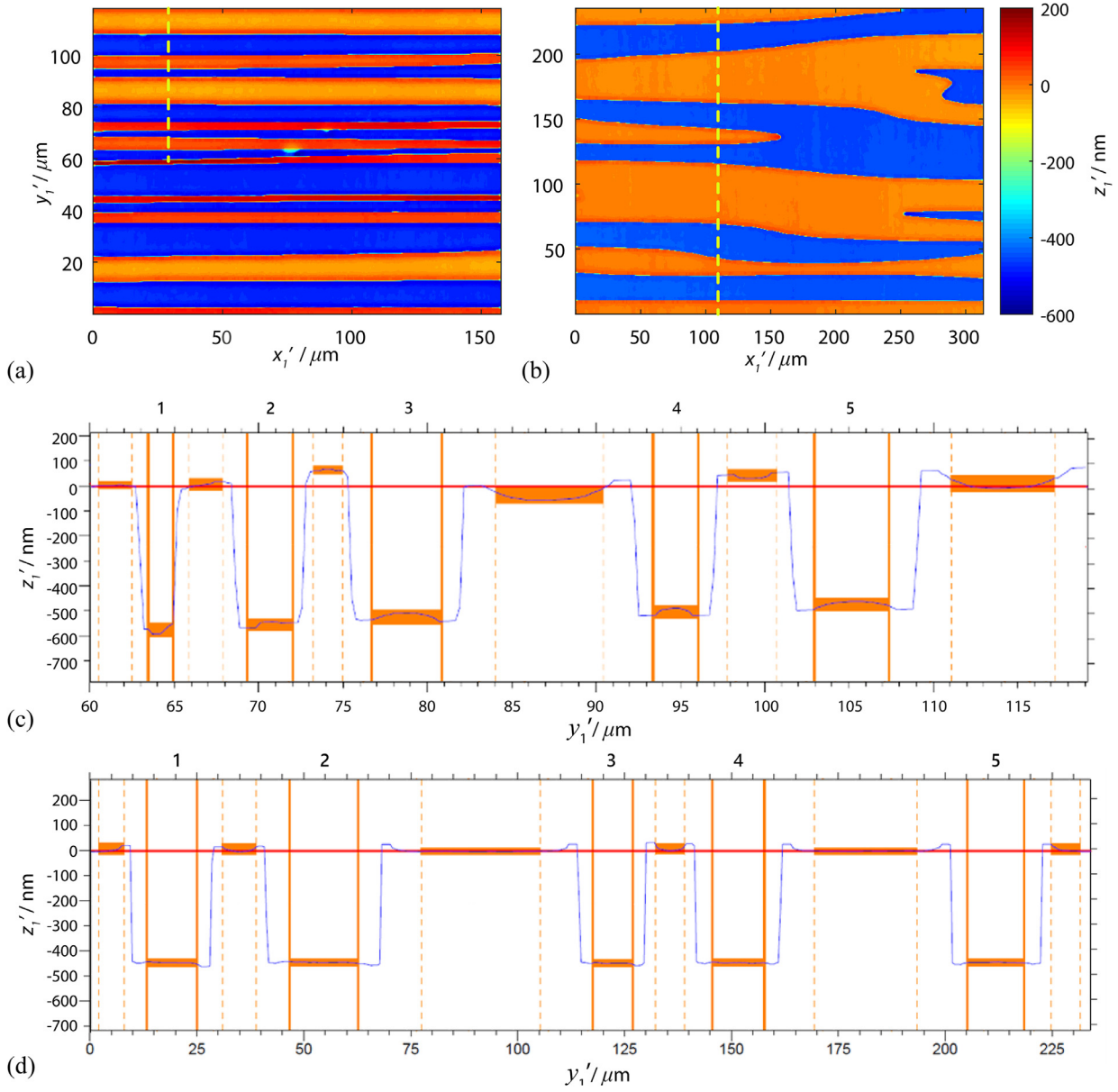

Fig. 1. Sub-regions of phase mask structures observed by CSI machine - Bruker NPFLEX. (a), (b) colour coded height maps for Masks A and B; (c), (d) cross sections of mask profile along the yellow dashed lines from (a) and (b).

tolithography and dry etching. Two masks were created, denoted Masks A and B, which were designed to produce PSF sizes of 1 × 256 and 4 × 64 digital micromirror device (DMD) pixels, respectively. In order to avoid diffraction artefacts, the lithographic patterns were generated initially as very high-resolution bitmap images (73,333 × 73,333 pixels) to cover an active area of 22 × 22 mm^2. Due to memory limitations with the photolithography machine (Heidelberg Instrument, DWL 66+), it was necessary to convert the original mask patterns from bitmap to GDSII vector format files.

The required step height (h) of the mask pattern was calculated according to Eq. (1), with the etching time varying accordingly:

$$h = \lambda_c/2(n_g - n_{air}) \tag{1}$$

where n_g and n_{air} are, respectively the refractive indices of the fused silica substrate and air. For the experimental setup used in this work, a blue LED light source with central wavelength λ_c = 460 nm along with a fused silica substrate n_g = 1.464 lead to a calculated step height thickness h = 495 nm. When $\lambda = \lambda_c$, the step height of the pattern then produces a phase shift of π rad between the portions of a wavefront passing through the two different thickness regions of the mask. Therefore, if the amplitude of the incident light is uniform across the wavefronts, and the areas of the two levels area equal, the forward-scattered on-axis light will interfere destructively and the resulting PSF will not have the DC peak. However, in reality, additional spectral components are present, so the phase shift value is not completely equal to π rad. Furthermore, Eq. (1) assumes normal incidence whereas in practice a range of angles will be incident on the mask. As a result, the DC peak always exists. This situation cannot be avoided, but its influence can be minimized by choosing a sufficiently narrow bandwidth light source.

One manufacturing option is to create the surface steps using the photoresist material itself, however control of the thickness of the photoresist layer, to the required precision of a few nm suggested by the simulations in Part 1, is challenging. The dry etching approach [2,3] is more controllable and was therefore adopted in this study. The manufacturing steps included (i) Spin coat: use a spin coater to produce a thin photoresist layer on the substrate surface, which is subsequently

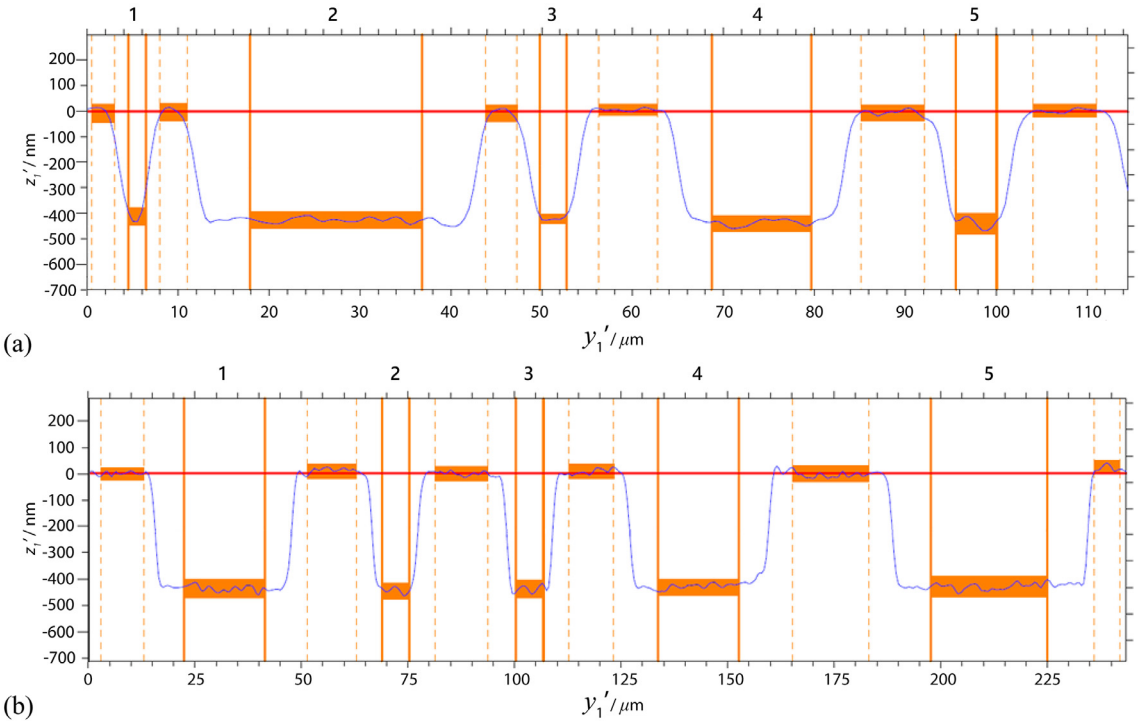

Fig. 2. Partial feature cross sections measured by the contact profiler. (a) Mask A and (b) Mask B.

baked at high temperature. (ii) Expose: use the photolithography machine to perform UV exposure of the desired pattern on the coating. (iii) Develop: wash off the unfixed parts of the photoresist with the solvent to leave the exposed part of substrate. (iv) Etch: etch the exposed substrate which has no photoresist to the desired depth. (v) Rinse and dry: wash away the rest of photoresist from the surface of the substrate to obtain the final product.

Inspection and analysis to determine the mask quality were then performed as follows. Firstly, the mask surface profile was measured via a non-contact coherence scanning interferometer (CSI) (Bruker, NPFLEX). The etched mask area is 22 × 22 mm^2, which is slightly larger than the illuminated region when the mask is placed in front of the projection lens. Nine sub-regions of the active area of the masks were selected. Fig. 1(a) and (b) show measured height maps from one such sub-region in Mask A and Mask B, respectively. The measurement of (a) used a 20 × lens magnification and a 2 × digital magnification, while (b) only used a 20 × lens magnification. The horizontal and vertical axes are denoted x_1' and y_1', respectively, the prime indicating a shift in the origin with respect to the (x_1, y_1) coordinate system of Fig. 2(c) of Part 1.

Fig. 1(c) and (d) show the cross sections of the areas marked by the yellow dashed lines in Fig. 1(a) and (b), respectively. As mentioned in the literature, when the height of the pattern steps is shorter than the coherence length of the light source, a 'batwing effect' (i.e., overshoot in apparent height adjacent to discontinuities) will be present [4]. The CSI used in this measurement has three light sources: white, green, and green with a narrow bandwidth. A white light source with a shorter central wavelength was selected for measurement to minimize the 'batwing' artefacts. As shown in Fig. 1(c) and (d), the blue curve represents the measured profiles of the cross sections. The data processing software (TalyMap Platinum 5.3) was used to isolate the 'islands' and 'valleys' of the captured profiles which are highlighted in orange, whilst excluding the 'batwing' affected zones. The red solid line represents the average 'island' height of the profile calculated from the top highlighted orange regions. Since the surface profile was manufactured using a subtractive etch process, we treat the red solid line as the baseline, the step heights are expressed with respect to this baseline. Step height measurements

Table 1
Partial feature size of Masks A&B measured by CSI.

Mask (magnification)	Dimension / μm					
	Location	1	2	3	4	5
A (20 × 2)	Depth	0.579	0.550	0.517	0.499	0.467
	Width	1.5	2.7	4.2	2.7	4.4
B (20 × 1)	Depth	0.445	0.444	0.447	0.446	0.445
	Width	11.8	16.2	9.3	12.3	13.2

Table 2
Partial feature size of Masks A&B measured by contact profiler.

Mask	Dimension / μm					
	Location	1	2	3	4	5
A	Depth	0.414	0.428	0.424	0.439	0.441
	Width	2	19	3	11	4.5
B	Depth	0.441	0.45	0.443	0.433	0.434
	Width	19	6.5	6.5	19	27.5

for each 'valley' region were calculated based on the mean depth in the orange zone. The measured dimensions from five sample valleys on these cross sections (numbered from 1 to 5) are listed in Table 1. The process was repeated using similar cross sections in nine sub-regions on each mask to estimate the overall mean step height. The mean step height estimated for masks A and B are 509 nm and 448 nm, respectively, which correspond to an error of around +3% and −9.5% from the target height of 495 nm.

In addition to the optical measurements, a contact profiler (Form Talysurf 2000) was used to perform a cross section measurement along one of the sides of the 22 × 22 mm^2 patterns for each mask. A portion of both cross sections are shown in Fig. 2. These do not have the bat-wing artefacts of the CSI measurements, but the measured steps appear to be rounded due to the finite radius of the stylus (2 μm). Table 2 shows the corresponding step-height values and widths in Fig. 2(a) and (b). By

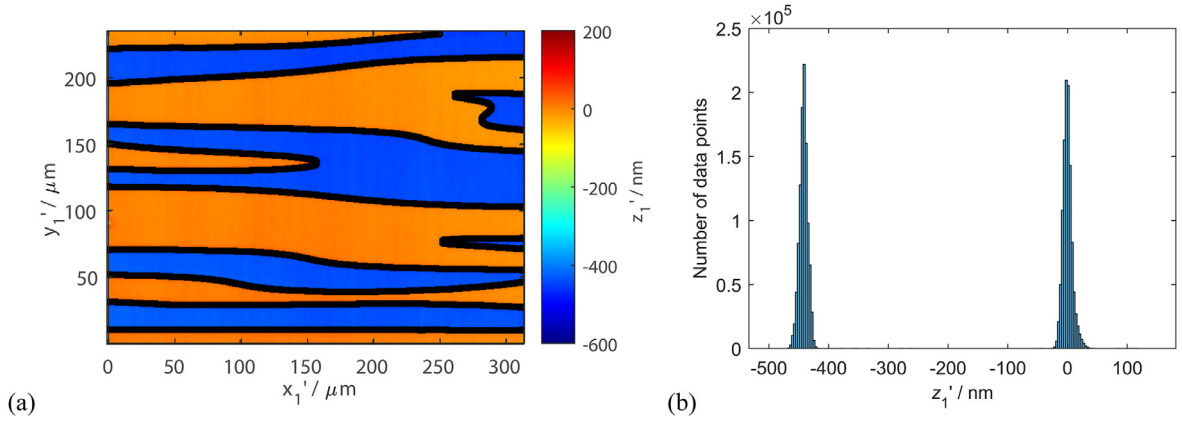

Fig. 3. (a) Height map from one sub-region of Mask B; (b) cumulative height histogram from all 9 sub-regions of Mask B.

averaging all the heights on the cross sections, the average step heights of the two masks were estimated as 425 nm and 439 nm, respectively, which correspond to an error of around −14.1% and −11.3% from the target height of 495 nm.

The CSI data was also used to check the ratio of areas corresponding to 'islands' and 'valleys'. This was done by defining a threshold height as the mean of the 9 height maps for each mask. The transition region between the 'island' and 'valley' can be located by finding the crossing points at this mean value. A fixed number of datapoints on either side of each transition mid-point are removed to eliminate the batwing-affected zones. The desired ratio can then be obtained by calculating the total number of pixels occupied by 'islands' and 'valleys'. The optimum ratio of 1:1 would ensure the lowest DC peak value.

Fig. 3(a) shows one of the 9 segmented region maps from Mask B. The orange areas represent the 'islands' and the blue areas are 'valleys', with the 'batwing' regions coloured black. Fig. 3(b) shows the cumulative measured height histogram after excluding batwing-affected regions, and combining samples from all 9 sub-regions of Mask B.

The resulting area ratio of 'islands' to 'valleys' from Mask B was calculated as 1.04:1. In addition, the difference in the mean heights of the 'island' and 'valley' regions was 447 nm, which is around 9.7% lower than the target height of 495 nm. The area ratio analysis was not feasible on the Mask A data due to the large size of the batwings in relation to the structure.

3. Experimental

3.1. Measurement of point spread function

Several experiments were carried out to evaluate the performance of the masks. The first was designed to measure the approximate size of the PSF of the projector's optical system with a mask placed immediately in front of the projection lens. The simplest way to do this was to look at the image generated from a single bright pixel. Although a single pixel is not a true point source, the size of the PSF is large in comparison to the pixel size, at least in the vertical direction. The schematic diagram of the experimental setup is shown in Fig. 4, and includes the projector (Vialux STAR-07) orientated with a small upward tilt such that the projector and camera optical axes were aligned, a phase mask, a frosted plastic plate to act as a diffuser, and a camera (Prosilica, GC1380H) with Nikon Zoom-Nikkor 35–70 mm f/3.3–4.5 AF lens. The phase mask was positioned parallel to the front of the projector lens mount using a custom support. The diffuser is a translucent circular plate, located on-axis between the camera and the projector. The distance (d_{13}) between the diffuser and the front of the projector lens was 0.5 m.

The camera recorded the image formed on the diffuser when the micromirror located at the centre of the DMD pixel array was set to 'on' and the rest to 'off'. In order to provide a suitable length scale the mask was then removed, and the camera captured a checkerboard image based on square regions of 64 × 64 DMD pixels. Examples of the captured images are shown in Fig. 5. Fig. 5(a) is the checkerboard pattern; (b) and (c) are the single-pixel patterns obtained using the Masks A and B, respectively. The top and bottom parts of Fig. 5(d), (e) and (f) show, respectively, horizontal and vertical cross sections through the images (a), (b) and (c), the legends in the corners indicating the cross sections' location. By using the scaling factor obtained using the checkerboard in (a), the sizes of the diffraction halo in (b) and (c) can be estimated as 1.9 × 259 DMD pixels and 4.5 × 65.9 DMD pixels, respectively. These are close to the target PSF dimensions of 1 × 256 DMD pixels and 4 × 64 DMD pixels, respectively, but are a little larger, most likely due to using a light source that was a pixel of finite size rather than a true point source.

In addition, Fig. 5(e) and (f) show that the intensity of the DC peak is significantly higher than the rest of the diffraction halo. To estimate the ratio of the DC peak intensity to the mean PSF intensity, 9 single-pixel projections were averaged to reduce noise. The average of all the intensity values within the diffraction halo, including the DC peak, were then calculated. The ratios of the DC peak intensity to average halo intensity of the two masks obtained by this method were 11.3:1 and 2.5:1 for Masks A and B, respectively. These are smaller than expected based on the analysis in Section 2.3 of Paper 1, which can again be attributed to the additional blur caused by the use of a single pixel source rather than a true point source.

3.2. Fringe projection

The quality of the generated sinusoidal fringe pattern was analysed by projecting different binary fringe images through each mask. The experimental system is shown in Fig. 6.

This system includes a high-speed projector, a phase mask mounted in front of the projection lens, a screen located at the image plane of the projector (O), and a camera viewing the screen off-axis. The projection distance was 0.5 m. The optical axis of the camera had an angle of 21° with respect to the projection axis, and the camera was focused on the centre of the screen. Additionally, electronic hardware synchronisation was used to ensure that the camera integration period corresponded to an integer number of projector frames.

The projected fringe quality was analysed by capturing image sequences based on (a) 8-bit sinusoidal fringes without a mask; (b) binary fringe images without a mask; (c) binary fringe images with Mask A and (d) binary fringe images with Mask B. The binary fringe patterns used in this experiment were generated by the random distribution method [1]. For all the experiments described in this paper, phase was computed from the intensity images using the standard 4-frame phase shifting for-

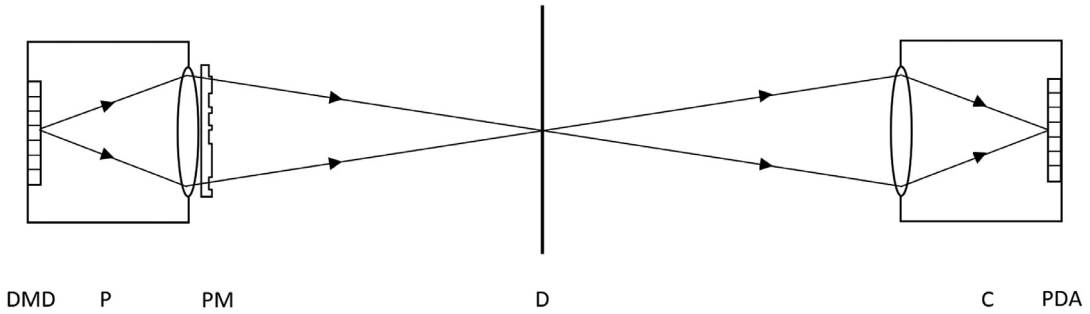

Fig. 4. Experimental setup to measure single pixel diffraction pattern from the phase mask, including digital micromirror device (DMD), projector (P), phase mask (PM), diffusing screen (D), camera (C) and photodetector array (PDA).

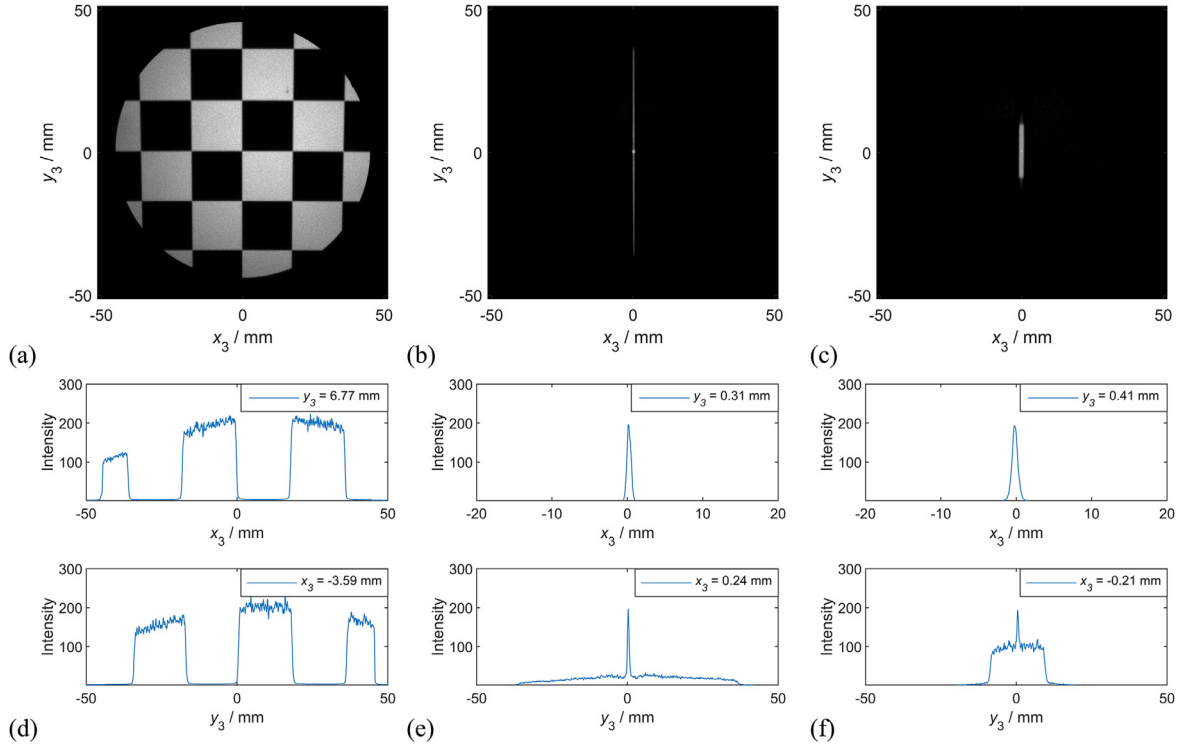

Fig. 5. Images of patterns projected onto diffuser for (a) 64 × 64 pixel checkerboard pattern; (b) and (c) single bright pixel projected through Masks A and B, respectively. (d), (e) and (f): horizontal (top row) and vertical (bottom row) cross sections from (a), (b) and (c) (intensity units: grey levels).

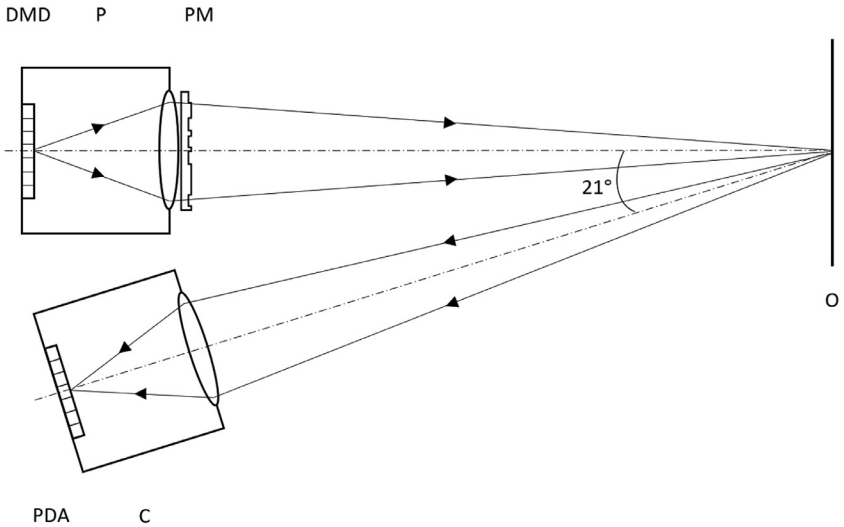

Fig. 6. Experimental setup to measure binary fringe patterns projected through the phase mask, including digital micromirror device (DMD), projector (P), phase mask (PM), screen (O), camera (C) and photodetector array (PDA).

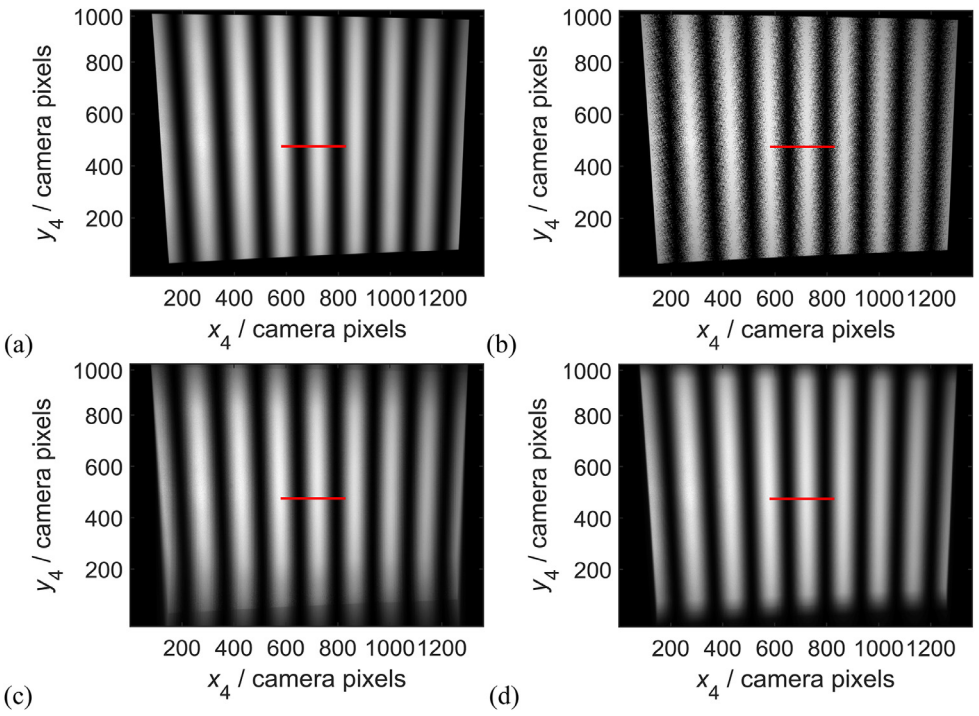

Fig. 7. Camera images based on projected pattern with 8 fringes across the projector field of view: (a) 8-bit greyscale pattern without mask; (b) 1-bit binary pattern without mask; (c),(d) 1-bit binary pattern with Mask A and Mask B, respectively. The red line (y_4 = 500) is the location of the intensity cross sections shown in Fig. 8.

mula, with $\pi/2$ phase shifts [1]. Although a phase shifting formula with smaller phase shifts would have reduced phase errors due to system nonlinearity [5], this would also have reduced the phase image acquisition rate, which is undesirable for dynamic applications. The image plane intensity depends on the number of 'on' bits within the PSF, which are chosen numerically and therefore we can expect negligible non-linearity on the projector side of the system. The Prosilica camera is a scientific grade digital CMOS camera with a linear intensity response. The overall system nonlinearity can therefore be seen to be relatively low, provided the sensor is not allowed to saturate for any of the acquired frames, and this is borne out by results presented later in the paper which suggest that random errors are the dominant error source rather than systematic errors such as nonlinearity.

Fig. 7 shows the first captured image in each case, from a sequence of phase-shifted patterns based on 8 fringes across the projector field of view. The x and y axes in the images, denoted x_4 and y_4, represent the intensity distribution across the image plane of the camera and are given in units of camera (PDA) pixels.

Fig. 8 shows a magnified view of each image from Fig. 7, together with a cross section from the red lines shown in the same figure. A comparison of Fig. 8(b) with (c) and (d) demonstrates the significant reduction in intensity fluctuations produced by the masks, to a level that is qualitatively similar to the 8-bit greyscale pattern in (a). There is however a reduction in image intensity, to approximately 84.2% and 89.6% of the 8-bit greyscale sinusoidal fringe image intensity for Masks A and B, respectively. The losses can be explained as being due to back-reflections of the light passing through the mask at each of the two air / glass interfaces. For normal incidence, the intensity reflection coefficient is predicted by the Fresnel equation [6] as

$$R = \left(\frac{n_g - n_{air}}{n_g + n_{air}} \right)^2 \tag{2}$$

Eq. (2) suggests 7.2% of the light incident normally on an air-glass-air interface combination will be back-reflected, though in practice the losses will be higher because R increases with increasing angle of the ray to the normal. An anti-reflection coating applied to the un-etched side of the phase mask could be used to reduce these losses.

Acquired images based on the phase-stepped reverse exponential fringe sequence [7] enable the phase gradient field to be calculated using the temporal phase unwrapping algorithm (as was performed in Part 1 [1] using simulated fringe patterns). However, selection of the image region to use for estimating unwrapped phase error differs here compared with that used for simulated data. Firstly, the acquired images include pixels that lie outside the projection area, which should be ignored. Secondly, the projected image which has passed through the mask is larger than the projected image without the mask due to convolution with the mask PSF. To compensate, the top and bottom margins of the projected image should be cropped by at least half of the PSF height, and the left and right margins of projected image should be cropped by at least half of the PSF width. We refer to the resulting region as the 'valid' projection area. Both projected images from Mask A and B were analysed using the same valid projection area to allow for direct comparison.

Fig. 9(a) shows the phase gradient image (i.e., the unwrapped phase map normalized to the range $-\pi$ to π rad) obtained from a 1-bit reverse exponential fringe pattern sequence with Mask A, using a maximum count of 8 fringes across the projector field of view. The left and right image margins correspond to surface points that lie outside the projector field of view and contain random intensity noise. Fig. 9(b) shows the valid projection area at the centre, with the black region corresponding to the area that is ignored. The phase error map shown in Fig. 9(b) was calculated by subtracting the obtained phase gradient map from the 5th degree polynomial fitted surface [1]. The standard deviation in phase error computed across the valid projection area is 1.80 mrad.

To observe the fringe quality throughout the measurement volume, the screen was translated over a distance of 0.4 m to 0.6 m in front on the projection lens, in increments of 0.05 m. Four phase-stepped reverse exponential fringe sequences were used based on a maximum fringe count of 32 fringes across the projector field of view: (a) 8-bit fringe pattern without mask; (b) 1-bit fringe pattern without mask; (c) 1-bit fringe pattern with Mask A; (d) 1-bit fringe pattern with Mask B. All 1-bit fringes were generated by the random distribution method. As before, to ensure comparability, the valid projection area for Mask A was applied to all captured images. Fig. 10 (data in Table 3) shows the standard deviation in the phase error at each projection distance. It can be seen that binary fringe patterns projected through the phase masks (i.e., groups (c) and (d)) had only minor variations in phase noise throughout the measurement volume. In addition, the phase masks significantly reduce the phase error compared to the binary defocused image, however, the

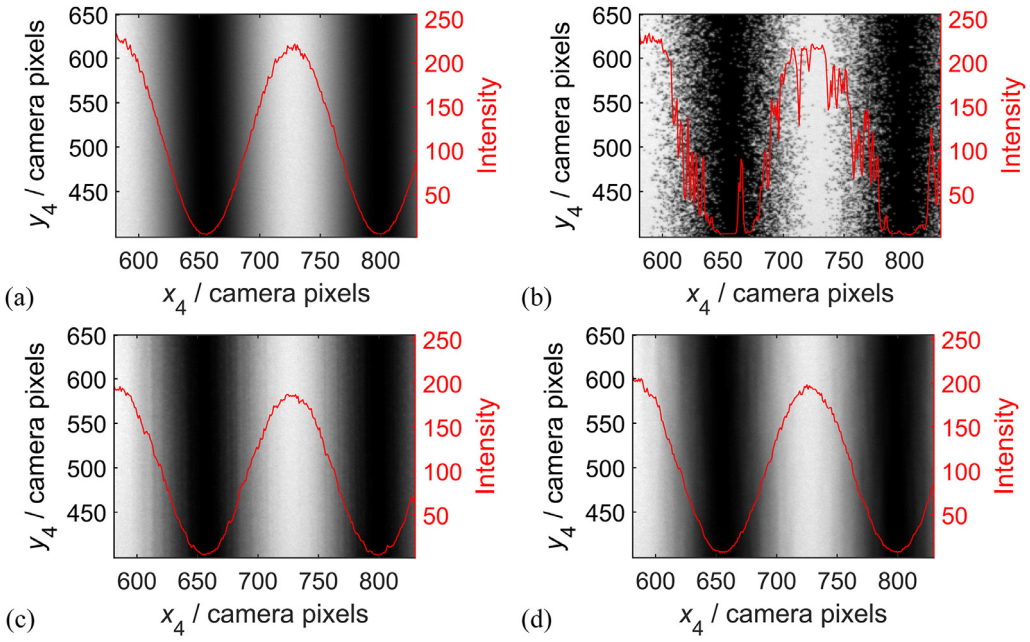

Fig. 8. (a) – (d) Magnified regions of the fringe patterns shown in Fig. 7(a) – (d), respectively. The red curves are the intensity profiles along the red lines from Fig. 7, in units of camera grey levels (right hand scale).

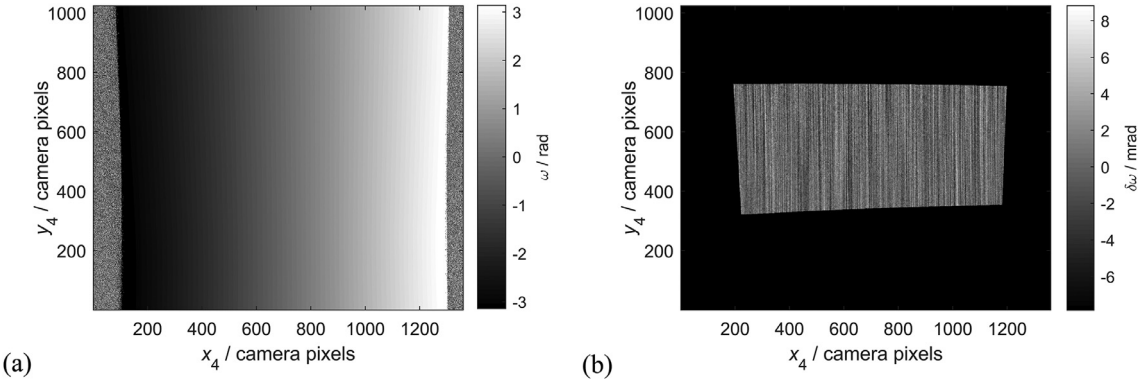

Fig. 9. (a) Phase gradient map $\omega(x_4, y_4)$ and (b) phase error (residuals) map $\delta\omega(x_4, y_4)$ based on 1-bit reverse exponential sequence of fringe patterns projected through Mask A, using a maximum count of 8 fringes across the projection field of view.

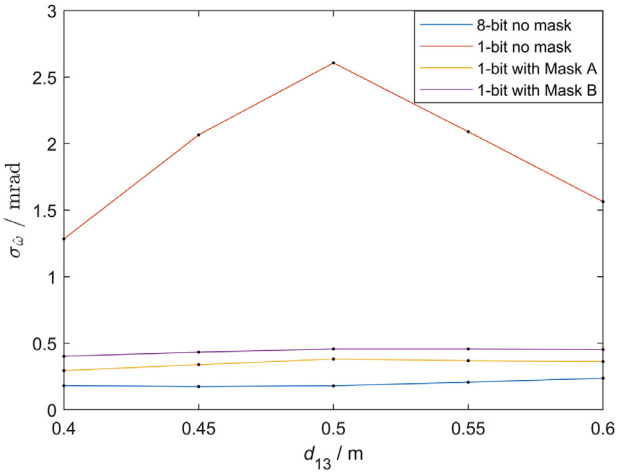

Fig. 10. Standard deviation of phase error, $\sigma_{\hat{\omega}}$, plotted against projection distance d_{13}, based on a phase-stepped reverse exponential fringe sequence using a maximum fringe count of 32 fringes across the projection field of view.

Table 3
Standard deviation of phase errors (Fig. 10 data).

Projection strategy	$\sigma_{\hat{\omega}}$ / mrad				
	40 cm	45 cm	50 cm	55 cm	60 cm
8-bit without mask	0.181	0.174	0.180	0.207	0.237
1-bit without mask	1.284	2.066	2.607	2.090	1.564
1-bit with Mask A	0.294	0.339	0.381	0.369	0.362
1-bit with Mask B	0.402	0.433	0.457	0.457	0.453

phase errors are still higher than those from 8-bit greyscale fringe patterns.

The second fringe design method proposed in Part 1 [1], the random tile method, was found in simulations to reduce the phase errors by at least an order of magnitude compared to those obtained using the random distribution method. It is therefore of interest to see whether the experimental phase errors can also be reduced by using the random tile method. Fig. 11 (data in Table 4) shows a comparison of the standard deviations of the phase error obtained by projecting binary images, generated by the two methods, through Mask B with the screen at a fixed distance of 0.5 m. The horizontal axis corresponds to the maxi-

Table 4
Standard deviation of phase errors (Fig. 11 data).

Projection strategy	$\sigma_{\hat{\omega}}$ / mrad					
	4-fringe	8-fringe	16-fringe	32-fringe	64-fringe	128-fringe
Tile method with Mask B	2.236	0.978	0.455	0.228	0.133	0.122
Distribution method with Mask B	4.720	2.080	0.931	0.462	0.260	0.217
8-bit without mask	1.893	0.800	0.350	0.166	0.091	0.071

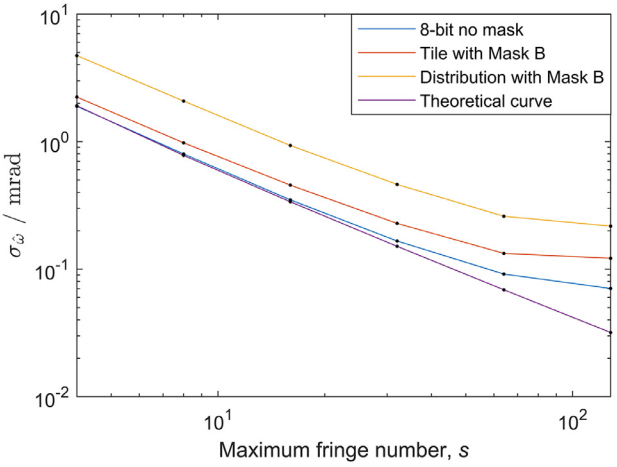

Fig. 11. Standard deviation of phase error, $\sigma_{\hat{\omega}}$, versus maximum reversed exponential fringe number s, for two binary fringe generation methods with Mask B, and for 8-bit greyscale fringes.

mum fringe count across the projector field of view used in the phase-stepped reversed exponential sequence. The graph also includes an 8-bit no-mask experimental phase error curve, and an analytical curve for the reversed exponential method [7].

It can be seen from Fig. 11 and Table 4 that the random tile method has reduced the phase error by about 50% compared to the random distribution method. As a result, the phase error values are much closer to those from the 8-bit greyscale sequences, with all of them except the highest fringe density lying within a factor of 1.18 × to 1.37 × of the greyscale phase errors. All three experimental curves are seen to deviate from the theoretical curve (Eq. (22) of Part 1). This is due, at least in part, to the systematic errors in the residual maps, $\delta\omega(x_4, y_4)$, which become increasingly apparent as the random phase errors are suppressed with increasing fringe density.

3.3. Distortion compensation

One of the important factors responsible for the increased phase noise with respect to the 8-bit fringe sequence is distortion of the projected image due to imperfections in the projector lens. The distortion causes misalignment of the fringes with respect to the projection system's PSF. As a result, the PSF kernel can straddle more than a small fraction of a fringe along its length, thus causing significant loss of contrast and hence increase in the noise of the calculated phase fields. The consequences of distortion are therefore particularly apparent when using a PSF with a large aspect ratio, and high-density fringe patterns.

The issue is illustrated in Fig. 12 with a binary pattern containing 64 fringes. A single acquired frame from the camera, with no mask on the projector, is shown in Fig. 12(a). Fig. 12(b) is an enlarged view of the red-framed area in (a). It is difficult to see the fringe distortion from these two pictures, because the overall distortion of the image caused by the off-axis camera viewing direction is more significant than the distortion from the projector lens. Fig. 12(c) is another captured image, with magnified portion in part (d), this time taken with Mask A in front of the projector. Fringes in the bottom corners have lower contrast due to the distortion mechanism described above. The reduction in contrast can be quantified by projecting four phase-shifted images from which the fringe modulation can be calculated on a pixel-wise basis. The dips in the resulting modulation map, Fig. 13(a), show the obvious distorting effect in those two corners.

To compensate for this loss, the pixels of the parallel-fringe image can be moved in the opposite direction at the fringe design stage. The resulting inverse pattern, after projection through the distorting lens, produces parallel fringes that are aligned with the PSF of the projection system. This solution can however be only implemented straightforwardly in the random distribution method since the random tile method requires the columns of the designed pattern to be parallel to the fringes.

The distorted fringe image is generated using a standard photogrammetric lens distortion model which includes keystone distortion, radial distortion [8] and tangential distortion [9]. The relevant equations are

$$\delta u_1 = k\left(u - u_C\right)\left(v - v_C\right) \tag{3}$$

$$r = \sqrt{\left(u - u_C\right)^2 + \left(v - v_C\right)^2} \tag{4}$$

$$\delta u_2 = \left(u - u_C\right)\left(p_1 r^2 + p_2 r^4 + p_3 r^6\right) \tag{5}$$

$$\delta u_3 = 2q_1\left(u - u_C\right)\left(v - v_C\right) + q_2\left[r^2 + 2\left(u - u_C\right)^2\right] \tag{6}$$

$$\delta\phi = \delta u_1 + \delta u_2 + \delta u_3 \tag{7}$$

In the above, (u, v) (which are shorthand notation for the variables $(\tilde{x}_m, \tilde{y}_n)$ in Paper 1) are the non-dimensional Cartesian coordinates of pixel (m, n) in the plane of the DMD; u_C and v_C are the coordinates of the centre of the projected image; k is the keystone correction coefficient; p_1, p_2, and p_3 are coefficients for radial distortion; q_1 and q_2 are coefficients for tangential distortion; δu_1 is the keystone deviation; δu_2 is the radial deviation; δu_3 is the tangential deviation; and $\delta\phi$ is the total distortion-induced change in the fringe phase used in Eq. (12) of Paper 1 [1].

The adjustable parameters ($k, p_1, p_2, p_3, q_1, q_2, u_C$ and v_C) were selected so that a pattern, containing thin lines that followed the fringe maxima, was blurred as little as possible when projected through the mask. Quantitatively, the optimal parameter configuration was achieved via a multi-dimensional unconstrained linear optimization, implemented using the MATLAB `fminsearch` function, in which a single pattern projection and image acquisition step was carried out within the main optimization loop. The thin binary lines of approximately 1–2 pixels wide were generated by thresholding the $C(m, n)$ matrix (Eq. (11) of Paper 1). A cost function was created as follows: a set of N_c uniformly spaced horizontal cross sections perpendicular to the fringes was extracted from the acquired image and the intensity peaks in each cross section due to the bright lines were identified automatically. For the jth peak in the kth cross section, the ratio of maximum intensity M_{jk} to the line width W_{jk} (defined as the full-width half-maximum) was calculated as:

$$E_{jk} = M_{jk}/W_{jk}, \tag{8}$$

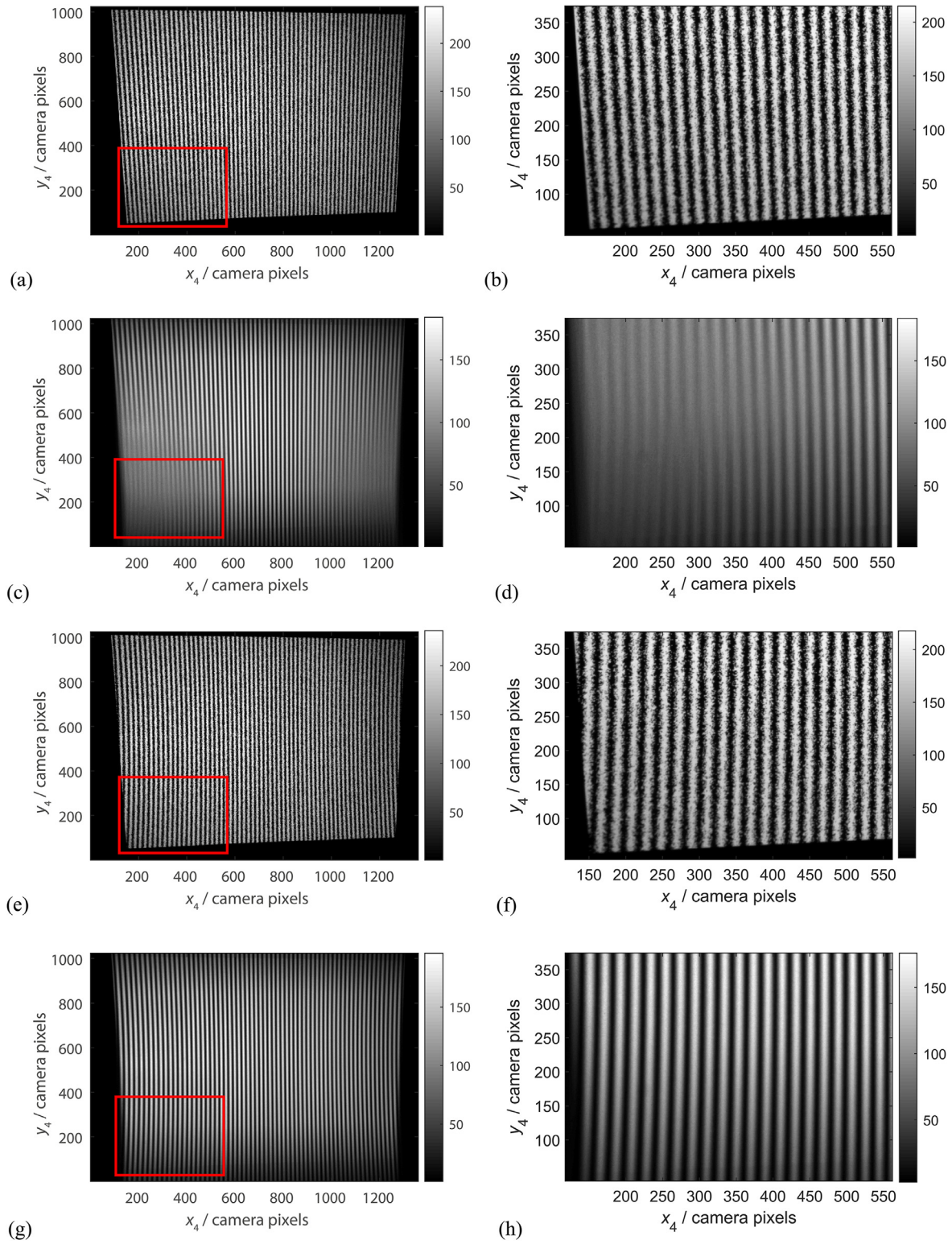

Fig. 12. Image of 64-fringe binary pattern projected onto a screen (a) without phase mask; (c) with Mask A; (e), (g): same as (a), (c), respectively, but with distortion compensation. (b), (d), (f), (h): enlargement of red-box region from (a), (c), (e), (g).

Table 5
Standard deviation of phase errors (Fig. 14 data).

Projection strategy	$\sigma_{\hat{\omega}}$ / mrad					
	4-fringe	8-fringe	16-fringe	32-fringe	64-fringe	128-fringe
Random distribution method with Mask A	4.236	1.802	0.814	0.412	0.386	384.187
Random distribution method with Mask A and distortion compensation	4.300	1.747	0.774	0.353	0.178	0.105
8-bit without mask	1.893	0.800	0.350	0.166	0.091	0.071

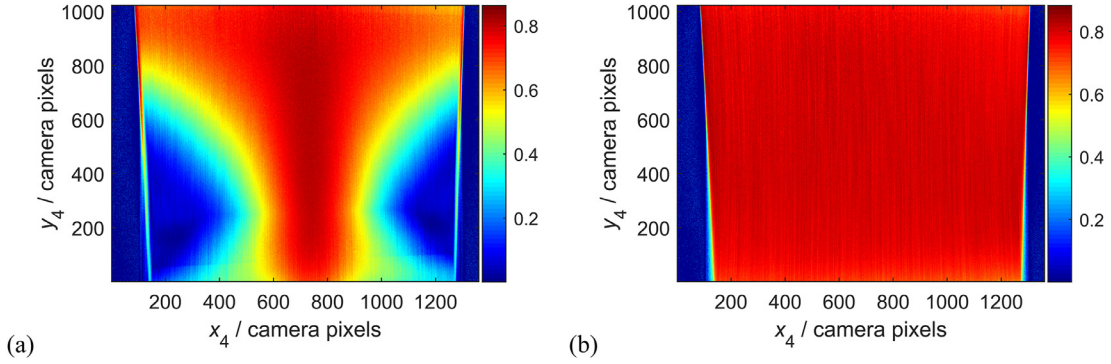

Fig. 13. Modulation maps for 64-fringe binary patterns with Mask A (a) without and (b) with distortion compensation.

from which the average ratio $\bar{E}$ is obtained:

$$\bar{E} = \frac{\sum_{j=1}^{N_k} \sum_{k=1}^{N_c} E_{jk}}{\sum_{k=1}^{N_c} N_k} \tag{9}$$

N_k is the number of peaks in the kth cross section, and N_c is the number of cross sections. The cost function to be minimized during the optimization was defined as $f = -\bar{E}(k, p_1, p_2, p_3, q_1, q_2, u_C, v_C)$.

The optimized parameter values were then used with the random distribution method to generate binary fringes with the required inverse distortion mapping. Fig. 12(e) shows a spatial distortion compensated pattern generated according to the distortion parameters obtained with Mask A. Fig. 12(f) is an enlarged image of the region inside the red box in (e). It can be seen that the fringes are no longer parallel to the edge of the projection area. Fig. 12(g) and (h) are equivalent images with the mask in place. A comparison of Fig. 12(h) with (d) shows the significant improvement in fringe contrast produced by the optimization procedure described above. The improvement can be quantified by calculating the modulation map from 4 phase-stepped images, which is shown in Fig. 13(b). This is now much more uniform across the field than was previously the case (Fig. 13(a)).

Fig. 14 (data in Table 5) shows a comparison of the standard deviation in phase error with and without fringe distortion correction, together with the corresponding curve for 8-bit greyscale patterns. The binary patterns were generated using the random distribution method and projected through Mask A. From Fig. 14, it is clear that the lens distortion has a large impact on images with high fringe density, in particular the 128-fringe data. The phase error of the image after distortion correction is significantly lower than before.

3.4. Multi-slice fringe projection

Experiments have also been carried out with the multi-slice random distribution method [1], to evaluate the scaling dependence of phase noise on the number of slices and maximum fringe density. Binary patterns were generated according to the algorithm in [1], and an image of the projected pattern for each was recorded by the camera. The required time integration was carried out as a post-processing step by summing the relevant camera frames. This emulates a procedure that would, in practical applications, be implemented in hardware to avoid extending the measurement duration, as was the case for the high-speed measurements described in the next section. Fig. 15 is an example from a 4-fringe sequence (i.e., four fringes across the projector field of view) generated based on 4 time slices. Fig. 15(a) shows small portions of the four acquired images with no phase mask; the bottom picture in Fig. 15(a) is the sum of the top four pictures. The image shown in Fig. 15(b) is similar to (a), except that Mask A was mounted in front of the projector lens. Fig. 16 shows the phase errors obtained with different numbers of time slices, with the individual error values listed in Table 6. The phase error curve for 8-bit greyscale patterns with no phase mask or distortion compensation applied is also added for reference. Fig. 16 illustrates that only 4 time slices are required to obtain a phase error lower than the achieved using a single 8-bit pattern, and that the phase error can be reduced by around 2 × for the 10-slice sequence.

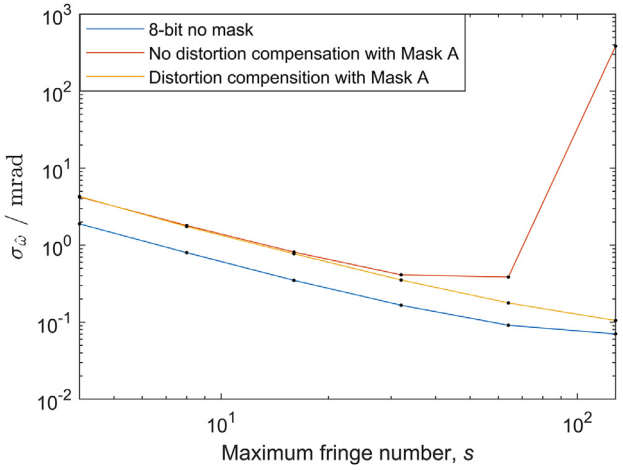

Fig. 14. Standard deviation of phase error, $\sigma_{\hat{\omega}}$, plotted against maximum fringe number s in the reverse exponential fringe sequence: comparison of binary fringes projected through Mask A with and without distortion compensation, and of 8-bit greyscale fringe patterns without phase mask.

4. High speed projection and acquisition

The proposed approach offers the potential to project sinusoidal fringe patterns at much higher frame rates than conventional 8-bit

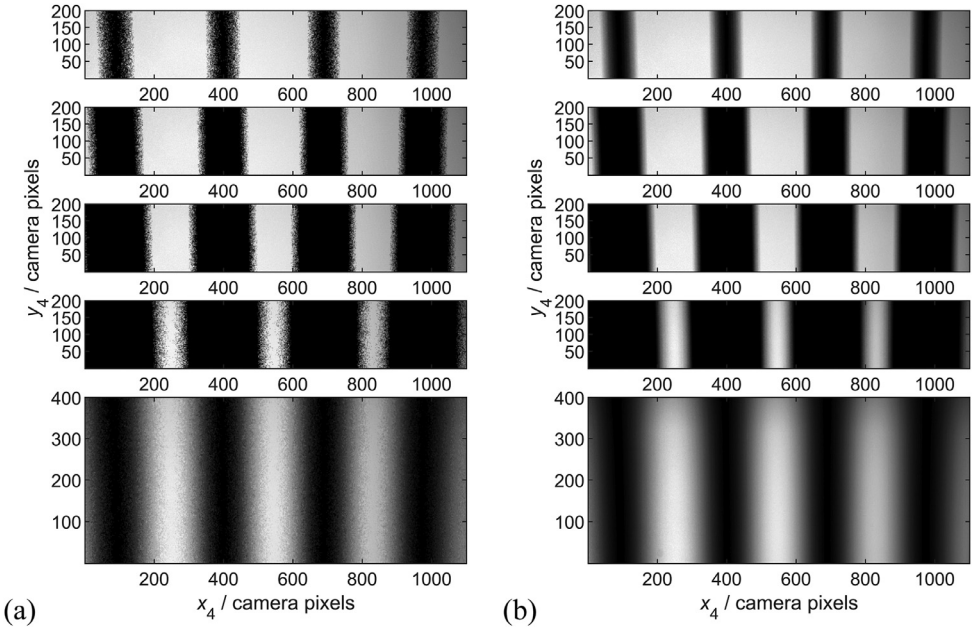

Fig. 15. Portions of images of the projected patterns from a 4-slice sequence with 4 fringes (see text for details). (a) without mask, (b) with mask A.

Table 6
Phase error of distortion compensated projections with Mask A, and different number of time slices (N_t) (Fig. 16 data).

Projection strategy	$\sigma_{\hat{\omega}}$ / mrad					
	4-fringe	8-fringe	16-fringe	32-fringe	64-fringe	128-fringe
$N_t = 1$	4.297	1.805	0.788	0.350	0.177	0.108
$N_t = 2$	2.261	1.000	0.423	0.201	0.102	0.065
$N_t = 4$	1.344	0.564	0.248	0.119	0.067	0.048
$N_t = 8$	0.826	0.354	0.158	0.079	0.050	0.041
$N_t = 10$	0.722	0.306	0.141	0.071	0.047	0.040
8-bit no mask	1.893	0.800	0.350	0.166	0.091	0.071

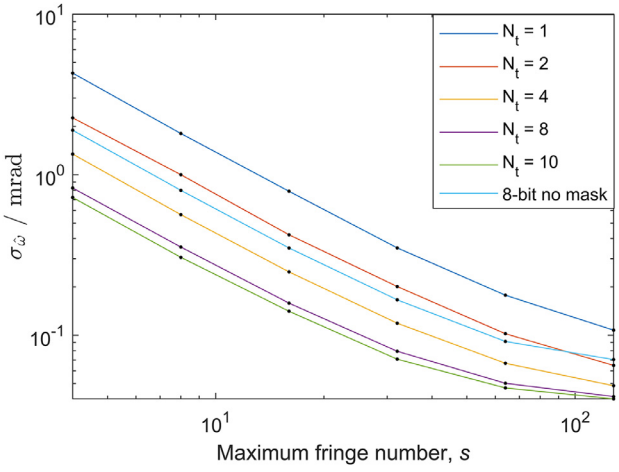

Fig. 16. Standard deviation of phase error versus maximum fringe number for multi-slice distribution method: effect of number of time slices (N_t).

greyscale projection methods. When combined with a high frame rate camera this enables fringe patterns to be acquired in dynamic environments that might otherwise not be possible (e.g. changing ambient lighting, moving surfaces, etc.).

This is demonstrated with a simple experiment to capture wrapped phase maps on a rotating discontinuous surface. Having demonstrated the fringe quality produced by the phase mask over an extended depth range in Section 3, an object with a restricted depth range – a 90 mm diameter DC cooling fan – was chosen here because of camera depth-of-field limitations arising from the maximum power output of the projector's LED (2.55 W). The fan was spray painted matt white, and controlled using a laboratory stabilised DC power supply. In order to demonstrate the quality of the acquired data at the maximum possible target velocity, results are presented in the form of wrapped phase maps, rather than shape. This is because computation of shape requires unwrapping through a number of phase maps (typically 5 or 6, requiring several tens of acquired images), and so would have required the rotation rate to be slowed down by the same factor to avoid significant phase unwrapping errors. For all the dynamic acquisitions, the fan's rotation rate was set to ca. 11 Hz, corresponding to a surface velocity of around 3.1 m s^{-1} at the circumference.

The fan surface was imaged using a Ximea xiB64 CB013MG-LX-X8G3-EF high-speed CMOS camera fitted with a Sigma 35 mm F1.4 DG HSM lens. The Ximea camera was synchronised to the Vialux projector using hardware triggers generated by the projector. Projection sequences were uploaded to the projector and computer memory pre-allocated for storing captured image sequences before starting the experiment. Projection sequences were based on sinusoidal fringe patterns with 32 fringes across the image, and $\pi/2$ rad phase step between consecutive frames. Wrapped phase maps were computed offline based on 4 consecutive acquired images.

The experiment compares three projection strategies denoted (i)–(iii), as described in Table 7. In method (i) the frame rate is constrained by the projector, which is using the native 8-bit greyscale mode. In method (ii) a higher frame rate is achieved by using the projector's native binary mode, but is constrained by the camera's maximum full-sensor frame rate. Finally, in method (iii), we utilise the multi-slice ap-

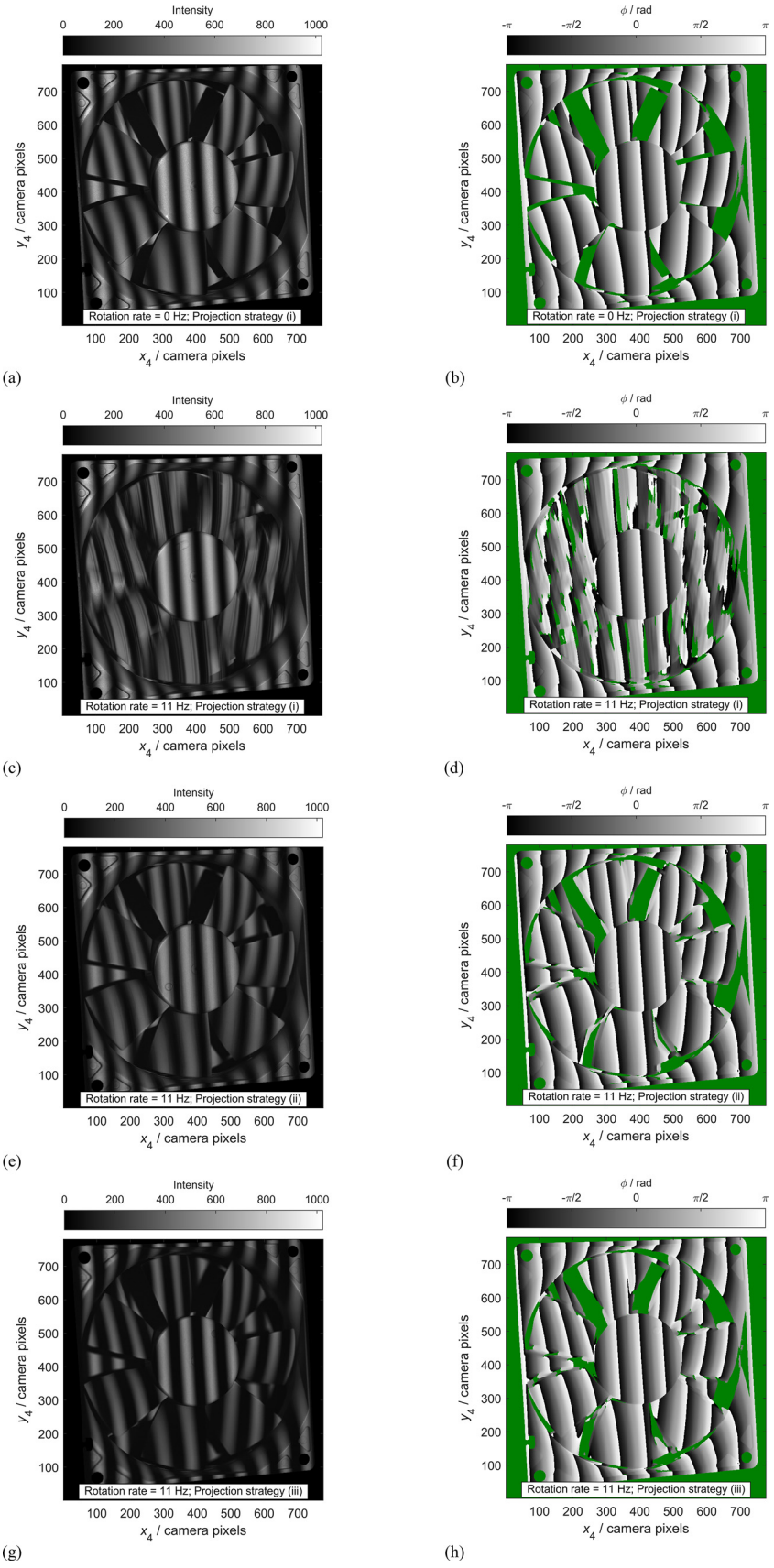

Fig. 17. Comparison of projection strategies (i)–(iii) for imaging a rotating fan surface. (a), (c), (e), (g) show cropped greyscale images extracted from the acquired image sequences (see text for details); (b), (d), (f), (h) show wrapped phase maps computed from 4 consecutive phase-stepped acquired images.

Table 7
Projection strategies.

Projection strategy	Mask	Fringe pattern	Distortion correction	Projector frame rate (s^{-1})	Camera frame rate (s^{-1})	Camera lens aperture
i	None	8-bit fringes	No	282	282	f/3.0
ii	B	1-bit with random distribution method	Yes	3650	3650	f/3.0
iii	B	1-bit with 4-slice random distribution method	Yes	14,493	3623	f/1.8

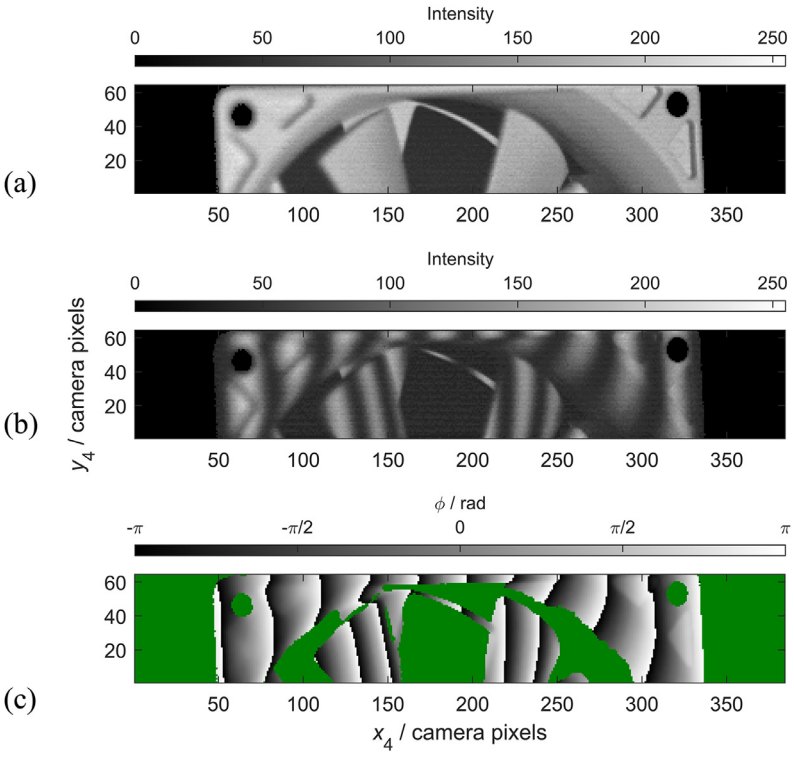

Fig. 18. Fan surface rotating at 11 Hz imaged at 9515 frames s^{-1}: (a) illuminated with uniform intensity; (b) illuminated with sinusoidal fringe pattern generated using Mask B and 1-bit pattern, based on random distribution method with distortion compensation applied, 32-fringes across the image; (c) wrapped phase map computed using 4 consecutive phase stepped acquired images.

proach to enable the projector to run at 4 × the camera's maximum frame rate, such that 4 projected patterns are integrated on the camera sensor per exposure period.

Results are summarised in Fig. 17, which shows cropped images from these experiments. The left column consists of single camera frames from a given sequence (units of greyscale); the right column shows wrapped phase maps, computed in each case from the image to its left and the three successive phase-shifted frames from the same sequence (units of radians). Regions with low fringe modulation are coloured green.

The first row of Fig. 17 was generated with the fan stationary and subsequent rows with the fan rotating. Rows 1 and 2 used projection strategy (i), with rows 3 and 4 using projection strategies (ii) and (iii), respectively. Projection strategy (i) works well on the stationary surface shown in (a) and (b): the phase wraps are smooth curves and the poorly-modulating (green) regions in (b) correspond to the gaps between the blades in (a). By contrast, when the fan is moving as in (c) and (d), the frame rate is too low to measure accurately the rotating surface. This is demonstrated by the striations in the phase wraps, and the poorly modulating regions that no longer correspond directly to the inter-blade gaps. At the fan circumference, the surface moves approximately 11 mm during each camera exposure period (equivalent to approximately 74 pixels), resulting in the significant blurring and phase errors visible in (c) and (d).

Projection strategies (ii) and (iii) perform much better, due to the increase in the acquisition frame rate by a factor of approximately 13 × . The resulting wrapped phase maps shown in (f) and (h), respectively, are qualitatively very similar, with only minor distortions apparent near the surface discontinuities. Potential benefits from the multi-slice approach used in projection strategy (iii) may have been offset by the reduction in projected light due to a fixed blanking period inserted between consecutive frames by the Vialux projector. The multi-slice approach inherently has more such blanking periods during each camera exposure period, and therefore required the camera lens aperture to be increased to compensate, resulting in a reduced depth of field.

In the previous experiment, the maximum acqusition frame rate was constrained by the camera, however, higher frame rates are possible when using the camera region of interest feature, which captures only a rectangular region on the sensor rather than the full surface area.

A second experiment was performed to image the fan surface rotating at 11 Hz using a camera sensor region corresponding to 384 × 64 pixels, with camera and projector frame rates locked at 9515 frames s^{-1} and camera lens aperture f/1.4. Mask B was used with a 1-bit projection sequence generated using the random distribution method, distortion compensation applied, 32 fringes across the image, with $\pi/2$ rad phase step between consecutive frames. Fig. 18 shows: (a) the rotating fan surface under uniform illumination; (b) the rotating surface illuminated by a single sinusoidal pattern extracted from the acquired image sequence; and (c) the resulting wrapped phase map computed from the four consecutive phase stepped acquired images. The experiment demonstrates that sinusoidal fringe patterns can be projected and captured at up to 9.5 kHz (limited only by the available hardware) using the proposed phase mask approach with 1-bit projection patterns, corresponding to an

increase in projection rate approaching two orders of magnitude when compared with conventional approaches based on 8-bit greyscale fringe pattern projection.

5. Summary

This paper has described the manufacture and evaluation of two binary phase masks (denoted A and B), designed according to the methods outlined in Part 1 [1]. The phase masks were designed to exhibit anisotropic PSF sizes of 1×256 and 4×64 pixels, respectively, and were manufactured using photolithography followed by dry etching. The resulting components were inspected using non-contact optical CSI and a mechanical contact profiler. Step height values were typically within 15% of the target value of 495 nm.

Experiments were performed to evaluate the influence of these phase masks on fringe projection. The first estimated the effective size of the optical PSF achieved by each mask; this was found to be within 1 DMD pixel of the nominal value in the horizontal direction and 3 DMD pixels in the vertical direction. The second experiment evaluated the relative performance of the masks when used with binary fringe patterns generated using several algorithms. The results indicate that (a) the phase mask approach can achieve significantly lower phase noise than the conventional defocus method described by previous authors, and which is furthermore more uniform over the measurement volume; (b) the random tile method can reduce the phase error by approximately 50% compared to the random distribution method; (c) image distortion correction can be applied alongside the random distribution algorithm to produce binary patterns that compensate for spatial distortion introduced by the projection optics, leading to significant improvements in the phase noise observed at high fringe densities; (d) observed phase error decreases as the number of time slices in the projection sequence increases, with approximately 50% reduction in phase error achieved for a 10-slice sequence compared with a traditional 8-bit greyscale sequence.

Finally, this paper also describes results from measurements of a moving surface that demonstrate that a phase mask combined with novel binary fringe patterns can achieve high-quality wrapped phase maps at image acquisition rates of up to 9515 frames s^{-1}.

Declaration of Competing Interest

We have no conflicts of interest to disclose.

CRediT authorship contribution statement

Wen Guo: Methodology, Software, Validation, Formal analysis, Investigation, Data curation, Writing – original draft, Writing – review & editing, Visualization. **C.R. Coggrave:** Methodology, Software, Validation, Data curation, Writing – review & editing, Visualization. **J.M. Huntley:** Conceptualization, Resources, Writing – review & editing, Supervision, Project administration, Funding acquisition. **P.D. Ruiz:** Resources, Writing – review & editing, Supervision.

Acknowledgments

The authors gratefully acknowledge financial support from the Engineering and Physical Sciences Research Council to the Future Metrology Hub (EP/P006930/1).

References

[1] Guo W, Huntley JM, Coggrave CR, Ruiz PD. High speed fringe projection for dynamic shape measurement using binary phase mask. Part 1: theory and simulation. Opt Lasers Eng 2022;154:107021.
[2] Levinson HJ. Principles of lithography. 2nd ed. Washington: SPIE press; 2005.
[3] Thompson LF. Introduction to microlithography. 2nd ed. Washington,DC: American Chemical Society; 1983.
[4] Harasaki A, Schmit J, Wyant JC. Improved vertical-scanning interferometry. Appl Opt 2000;39(13):2107–15.
[5] Coggrave CR, Huntley JM. Optimization of a shape measurement system based on spatial light modulators. Opt Eng 2000;39(1):91–8.
[6] Hecht E. Optics. 4th ed. San Francisco: Addison Wesley; 2002.
[7] Huntley JM, Saldner HO. Error-reduction methods for shape measurement by temporal phase unwrapping. J Opt Soc Am A 1997;14(12):3188–96.
[8] Schreiber W, Notni G. Theory and arrangements of self-calibrating whole-body three-dimensional measurement systems using fringe projection technique. Opt Eng 2000;39(1):159–69.
[9] Heikkilä J, Silvén O. A four-step camera calibration procedure with implicit image correction. In: Proceedings of IEEE Computer Society Conference on Computer Vision and Pattern Recognition, 14; 1997. p. 1106–12.